ACCURACY OF LOW REYNOLDS NUMBER COMPUTATIONS USING INCOMPRESSIBLE SPH

Jason P. Hughes[1], David I. Graham[2]

[1] School of Mathematics and Statistics, University of Plymouth, Plymouth, Devon, PL4 8AA, UK. Tel +44(0)1752 232725; Fax +44(0)1752 232780;E-mail jhughes@plymouth.ac.uk,
[2] School of Mathematics and Statistics, University of Plymouth, Plymouth, Devon, PL4 8AA, UK. Tel +44(0)1752 232746; Fax +44(0)1752 232780;E-mail dgraham@plymouth.ac.uk

ABSTRACT

This paper reports the results of incompressible smoothed particle hydrodynamics (I-SPH) computations of very low Reynolds number lid-driven cavity flow. In this case, particles can be 'frozen' and the method can be viewed as a fixed grid method. I-SPH is a two-step predictor-corrector projection method. An explicit predictor integrates the contributions from viscous and body forces. An implicit corrector then updates the velocity by adding a curl-free contribution that is proportional to the pressure gradient. An intermediate step requires the solution of a pressure Poisson equation with boundary conditions of zero normal gradients on solid surfaces. Here, three different formulations are used to implement these conditions and the results compared and contrasted. A convergence study is carried out for each of the three boundary formulations and for two ratios of smoothing length to inter particle spacing ($h/dx =$ 1, 1.2). Results for 10x10, 17x17, 25x25, 35x35, 50x50, 75x75 and 100x100 particles are presented and the 'error' characterised as a function of the inter-particle spacing.

KEYWORDS SPH; Pressure Poisson equation; Boundary Conditions; Low Re

1. INTRODUCTION

SPH is a very flexible and powerful numerical method that has recently been applied to a large range of industrial, engineering and environmental fluid flows (Monaghan & Kos (1992), Cleary et al (2002), for example). One of the main features is its Lagrangian particle-tracking approach which allows the method to cater for very large deformations such as those occurring in wave breaking, sloshing, mould-filling and hypervelocity impacts, for example.

There are two main variants of SPH for incompressible flows. One uses a 'stiff' equation of state to relate pressure to density in a 'weakly compressible' variant of traditional SPH. The second imports the idea of pressure-correction from grid methods – giving rise to a family of I-SPH methods.

From the SPH literature, however, it is apparent that even within these two variants of SPH, there is large variation in practice, for example in choosing smoothing functions and smoothing lengths. In particular, there appear to be several methods in use for implementing boundary conditions on solid walls. It is not always clear from the literature what are the relative advantages and disadvantages of the various formulations, and certainly no consensus has yet been reached over which is the best choice for a given problem.

In the zero-Reynolds number limit, the Lagrangian acceleration $D\boldsymbol{u}/Dt$ approaches the Eulerian one $\partial\boldsymbol{u}/\partial t$ as the nonlinear convection terms that normally appear in Eulerian formulation of the acceleration are negligible. In this case, SPH methodology can be applied to a 'frozen' particle configuration i.e. one where particles are not allowed to move as they would in the vast majority of SPH computations. Indeed, it is normally the motion of the particles and the consequent deformability that provides SPH with practical advantages over

traditional grid methods. However it is instructive to study the frozen particles case, which can then be viewed as a traditional grid method and analysed as such. As noted above, the comparison is valid for low Reynolds number. This case provides checks of several aspects including (i) pressure boundary conditions; (ii) stability, (iii) accuracy of the SPH interpolation viewed as a grid method and (iv) degradation of numerical results due to particle motion.

The test problem upon which we base our investigation is the lid-driven cavity flow. This case provides a very popular test for numerical viscous flow models. Recently, it was chosen as a test-case for the first SPHERIC Workshop (Rogers et al (2006)), and several SPH codes took up the challenge. Most of the codes were traditional weakly-compressible versions of SPH, with only one I-SPH contribution from the group at the University of Manchester. The workshop focussed upon relatively high Reynolds number flow in the range 100-10,000. This paper complements this test case by examining the performance of another version of I-SPH in simulating this flow. However, our main focus is the behaviour at very low Reynolds number. It is noted that low-Reynolds number SPH simulations were carried out by Morris et al (1997), where they considered Couette and Poiseuille flows. We determine convergence behaviour for a number of different formulations of the pressure Poisson equation and in particular for three different methods for implementing the zero-gradient boundary conditions that arise.

2. FORMULATION

2.1 LID-DRIVEN CAVITY FLOW

The flow configuration is illustrated in Figure 1. The flow starts from rest, and accelerates under the influence of the lid, which is instantaneously moved at uniform speed horizontally. Eventually, a steady state is reached.

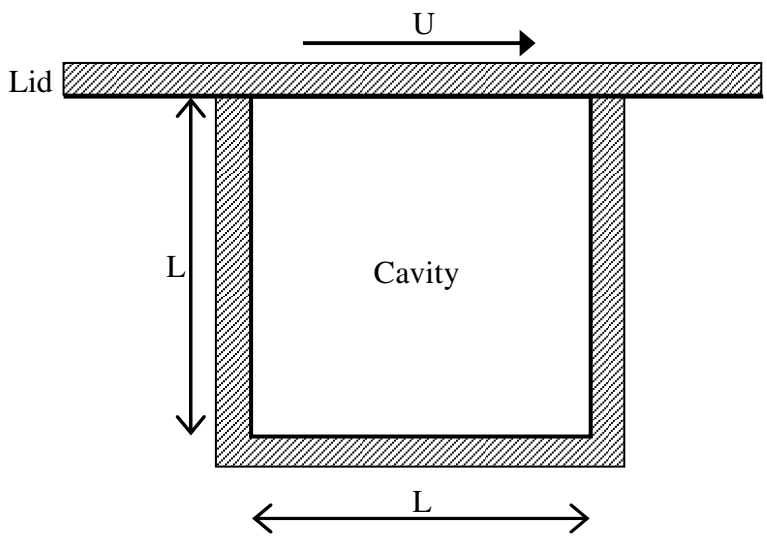

Figure 1: Lid-driven cavity configuration

The governing equations are the usual Navier-Stokes equations:

$$\frac{D\boldsymbol{u}}{Dt} = -\frac{1}{\rho}\nabla P + \boldsymbol{g} + \nu\nabla^2\boldsymbol{u}\,, \qquad [1]$$

$$\frac{1}{\rho}\frac{D\rho}{Dt} + \nabla\cdot\boldsymbol{u} = 0\,. \qquad [2]$$

In truly incompressible flow, of course, $D\rho/Dt$ is zero and $\nabla \cdot \boldsymbol{u} = 0$. In SPH, however, the numerical solution is not exactly incompressible and we make use of equation [2].

2.2 INCOMPRESSIBLE SPH MODEL

Following Chorin (1967) and Cummins & Rudman (1999), the idea of the incompressible SPH model is that the velocity vector can be decomposed into the sum of divergence-free and curl-free parts. The decomposition is as follows:

$\boldsymbol{u} = \boldsymbol{u}_* - \boldsymbol{u}_{**}$, where $\boldsymbol{u}$ is divergence-free $\boldsymbol{u}_*$ is any arbitrary velocity field and $\boldsymbol{u}_{**}$ is curl-free.

I-SPH is a two-step pressure-correction model to solve equations [1] and [2]. The prediction step solves the viscous problem

$$\frac{D\boldsymbol{u}_*}{Dt} = \nu\nabla^2\boldsymbol{u} + \boldsymbol{g}\,, \qquad [3]$$

subject to the conditions that $\boldsymbol{u}_*$ has fixed values on solid boundary surfaces. In practice, the viscous term $\nu\nabla^2\boldsymbol{u}$ is approximated by using the velocity distribution at the end of the previous time step, so the viscous step is explicit.

$\boldsymbol{u}_*$ is then an arbitrary velocity field (i.e. it is neither divergence-free nor curl-free). The incompressible velocity field $\boldsymbol{u}$ is found by subtracting away the curl-free part, $\boldsymbol{u}_{**}$. Subtracting [1] from [3], the equation for $\boldsymbol{u}_{**}$ becomes:

$$\frac{D\boldsymbol{u}_{**}}{Dt} = \frac{1}{\rho}\nabla P\,, \qquad [4]$$

(and clearly $\boldsymbol{u}_{**}$ is curl-free since the curl of a gradient is zero). In order to find $\boldsymbol{u}_{**}$, the pressure field must first be solved for. Taking the divergence, we get the following Poisson-type equation:

$$\nabla \cdot (\frac{1}{\rho}\nabla P) = \frac{D}{Dt}\left[\nabla.\boldsymbol{u}*\right]. \qquad [5]$$

The Poisson equation is subject to boundary conditions $\partial P/\partial n = 0$ on solid surfaces (which arises from the fact that $\boldsymbol{u}_*$ and $\boldsymbol{u}$ have the same fixed values on solid surfaces thus their difference is zero. Having found the pressure, $\boldsymbol{u}_{**}$can also be found and the final, incompressible, velocity $\boldsymbol{u} = \boldsymbol{u}_* - \boldsymbol{u}_{**}$ can be evaluated.

2. 3 SPH IMPLEMENTATION

2.3.1 VISCOUS STEP

As noted above, the explicit predictor step integrates equation [3] to give

$$\Delta\boldsymbol{u}_* = (\boldsymbol{g} + \nu\nabla^2\boldsymbol{u}_t)\Delta t\,, \qquad [6]$$

where subject to fixed velocities on solid boundaries. This then defines intermediate particle velocities and positions:

$$\boldsymbol{u}_* = \boldsymbol{u}_t + \Delta\boldsymbol{u}_* \qquad [7]$$

$$\boldsymbol{r}_* = \boldsymbol{r}_t + \boldsymbol{u}_* \Delta t \,. \qquad [8]$$

In the above, $\Delta \boldsymbol{u}_*$ is the change in particle velocity during the prediction step, Δt is the time increment, $\boldsymbol{u}_t$ and $\boldsymbol{r}_t$ are the particle velocity and position at time t and $\boldsymbol{u}_*$ and $\boldsymbol{r}_*$ are the intermediate particle velocity and position.

2.3.2 PRESSURE POISSON EQUATION

As an intermediate step, the pressure distribution must be determined. This is found by solving the discrete form of the Pressure Poisson equation:

$$\nabla \cdot (\frac{1}{\rho_*} \nabla P_{t+\Delta t}) = \frac{1}{\Delta t} \nabla . \boldsymbol{u}_* \qquad [9]$$

subject to zero-gradient conditions on solid boundaries. This is an implicit equation which is discretized in matrix form and the matrix equation solved using a biconjugate gradient method (Press *et al* (1992), p77) to find $P_{t+\Delta t}$, the particle pressure at time $t + \Delta t$.

2.3.3 PRESSURE-CORRECTION

The resulting pressure is used to update the particle velocity and position:

$$\boldsymbol{u}_{**} = \frac{1}{\rho_*} \nabla P_{t+\Delta t} \Delta t \qquad [10]$$

$$\boldsymbol{u}_{t+\Delta t} = \boldsymbol{u}_* - \boldsymbol{u}_{**} \qquad [11]$$

where $\boldsymbol{u}_{**}$ is the curl-free component of the particle velocity found during the correction step, ρ_* is the intermediate particle density after the prediction step and $\boldsymbol{u}_{t+\Delta t}$ is the particle velocity at time $t + \Delta t$. The final particle position is given by

$$\boldsymbol{r}_{t+\Delta t} = \boldsymbol{r}_t + \frac{(\boldsymbol{u}_t + \boldsymbol{u}_{t+\Delta t})}{2} \Delta t \qquad [12]$$

where $\boldsymbol{r}_t$ and $\boldsymbol{r}_{t+\Delta t}$ are the position of a particle at time t and $t + \Delta t$.

2.3.4 SPH APPROXIMATIONS

For completeness, we list the SPH approximations used in the computations reported in this paper. In doing so, we follow the work of Shao *et al* (2006) whose code we have inherited and modified, and whose notation we have followed.

Density $$\rho_a = \sum_b m_b W(|\boldsymbol{r}_a - \boldsymbol{r}_b|, h) \qquad [13]$$

Pressure gradient $$(\frac{1}{\rho} \nabla P)_a = \sum_b m_b (\frac{P_a}{\rho_a^2} + \frac{P_b}{\rho_b^2}) \nabla_a W_{ab} \qquad [14]$$

Divergence $$\nabla \cdot \boldsymbol{u}_a = \rho_a \sum_b m_b (\frac{\boldsymbol{u}_a}{\rho_a^2} + \frac{\boldsymbol{u}_b}{\rho_b^2}) \cdot \nabla_a W_{ab} \qquad [15]$$

Pressure Laplacian $$\nabla \cdot (\frac{1}{\rho} \nabla P)_a = \sum_b m_b \frac{8}{(\rho_a + \rho_b)^2} \frac{P_{ab} \boldsymbol{r}_{ab} \cdot \nabla_a W_{ab}}{|\boldsymbol{r}_{ab}|^2} \qquad [16]$$

Viscosity $$(\nu\nabla^2\boldsymbol{u})_a = \sum_b m_b \frac{4(\mu_a+\mu_b)}{(\rho_a+\rho_b)^2}\frac{\boldsymbol{u}_{ab}\boldsymbol{r}_{ab}\cdot\nabla_a W_{ab}}{|\boldsymbol{r}_{ab}|^2} \quad [17]$$

In the above, approximations are defined at particle a, whose neighbours are particles b, m_b is the particle mass, μ is the viscosity, ρ is the density, P is pressure, $\boldsymbol{r}$ is the position vector and $\boldsymbol{u}$ is velocity. The smoothing length is h and φ_{ab} is $(\varphi_{\underline{a}} - \varphi_{\underline{b}})$ for any scalar or vector quantity φ. We utilise a cubic spline kernel function W_{ab}, as used by Shao and Lo (2003).

In the case of constant density and viscosity when using regularly-spaced, fixed particles, the SPH approximations [16] and [17] can be analysed using Taylor series. It is found that, when $h=dx$, the right-hand side of [16] gives $1.012227083\nabla^2 P/\rho + O(dx^2)$. When $h=1.2dx$, this becomes $0.9910335789\nabla^2 P/\rho + O(dx^2)$. Thus, although the approximations are not 'consistent' in the sense that they do not converge to the exact value of the Laplacian as $dx\rightarrow 0$, the nett effect in the current case is simply to modify the density and viscosity. This could in principle be corrected but since the modifications in density and viscosity are only of the order of 1%, no correction is applied here.

2.3.5 PRESSURE BOUNDARY CONDITIONS

To implement the pressure boundary condition $\partial P/\partial n = 0$, we have used three different implementations.

Method 1: Implicit wall pressures. We solve for the pressures at wall particles. The SPH equations for wall particles and those near walls include dummy particles but we assume that the pressures at dummy points (which are placed along outward-pointing wall normal vectors emanating from a given wall particle) will be the same as those located at the associated wall particle (see Figure 2).

Method 2: Explicit wall pressures. We follow the approximate method described by Lee *et al* (2006). For a given point on the boundary, we associate a fictitious point in the interior of the flow, at a normal distance d from the wall point (see Figure 2). We find the pressure at the interior point (at time t, using the SPH approximation) and then set the pressure at the wall point and the two layers of exterior dummy particles (time $t+\Delta t$) equal to this pressure.

Method 3: Explicit dummy pressures, but solve to wall. In this case, the method is similar to Method 2 (see figure 2) except that wall pressures are solved for and the pressures of dummy particles are set equal to the wall pressure from the previous timestep.

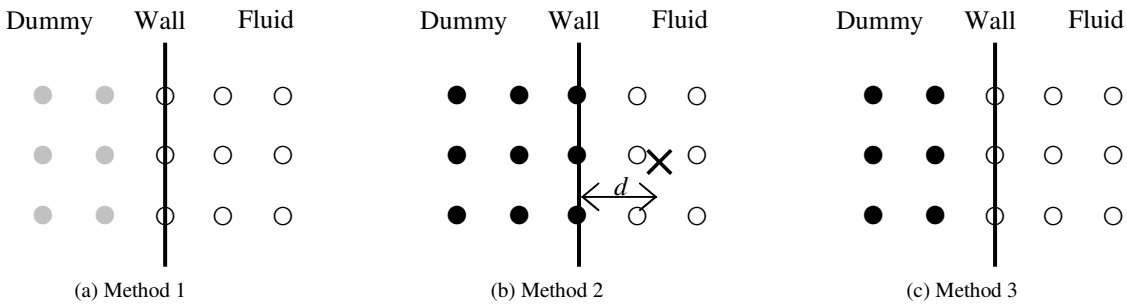

Figure 2 (a,b,c): Boundary conditions for methods 1, 2 and 3. ○ – denotes particle at which pressure is solved for at time $t+\Delta t$, ● – denotes particle at which pressure is set using solution values at time $t+\Delta t$ ● – denotes particle at which pressure is set using solution values at time t, ✕ - denotes fictitious point at which SPH interpolated value of pressure is evaluated for method 2.

3. COMPUTATIONAL RESULTS

In order to compare the effectiveness of each of these three boundary implementations, we solve the lid-driven cavity flow at very small Reynolds number. The great advantage of this case is that the solution attains a steady-state before the particles have moved appreciably (and in practice we fix the particles and get the zero-Reynolds number result). Initially, the velocities of wall and dummy particles on the top lid are set equal to (1,0) and the velocities of all other particles are set to zero. The lid then drives the flow, which continues to develop until a steady-state is found. Development of velocity profiles is shown in Figure 3. For a Reynolds number of 0.001, fully-developed solutions are found at around 0.0001s (results were computed up to 0.0004s and showed no change beyond 0.0001s). The fully-developed velocity vectors and streamlines are shown in Figure 4 (and note that the particles are frozen so that they are still in their initial spatial configuration).

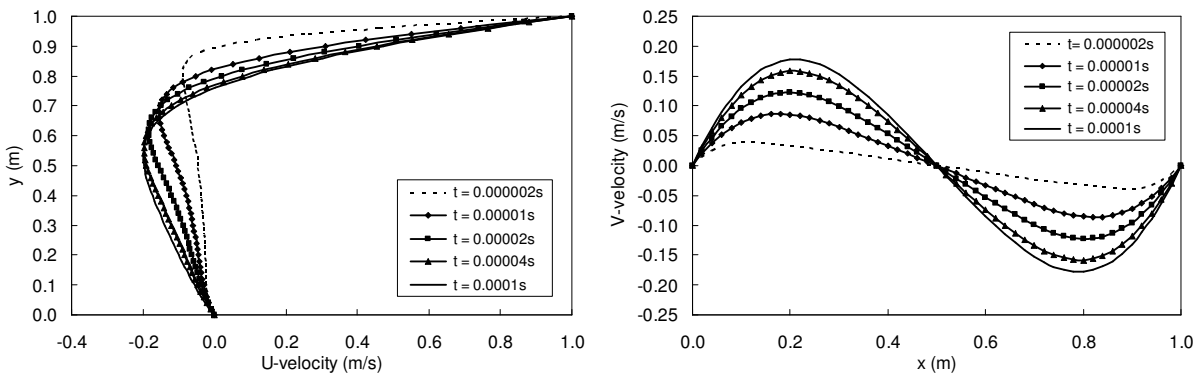

(a) $x = 0.5$ (b) $y = 0.5$

Figure 3 (a,b): Development of velocity profiles.

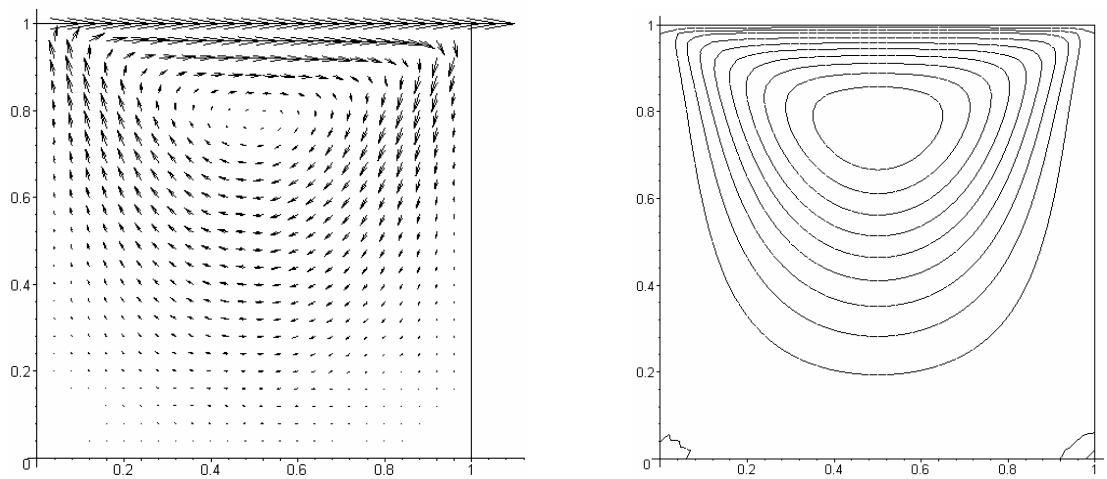

Figure 4 (a,b) a: Velocity vectors b: streamlines

We now investigate convergence behaviour for each of the three wall pressure boundary conditions and for two different ratios of smoothing length h to inter-particle distance *dx*. We carry out the computations on 10x10, 17x17, 25x25, 35x35, 50x50, 75x75 and 100x100-particle systems. Figure 5 (a [Method 1], b [Method 2]) shows the behaviour of the *y*-component of velocity along the cavity centreline $y = 0.5$. Clearly, the results appear to

converge, and converge to the same result for each implementation, though the approach to convergence is different in each case. Note that the results for Method 3 were found to be the same as for Method 1 and thus are not plotted here.

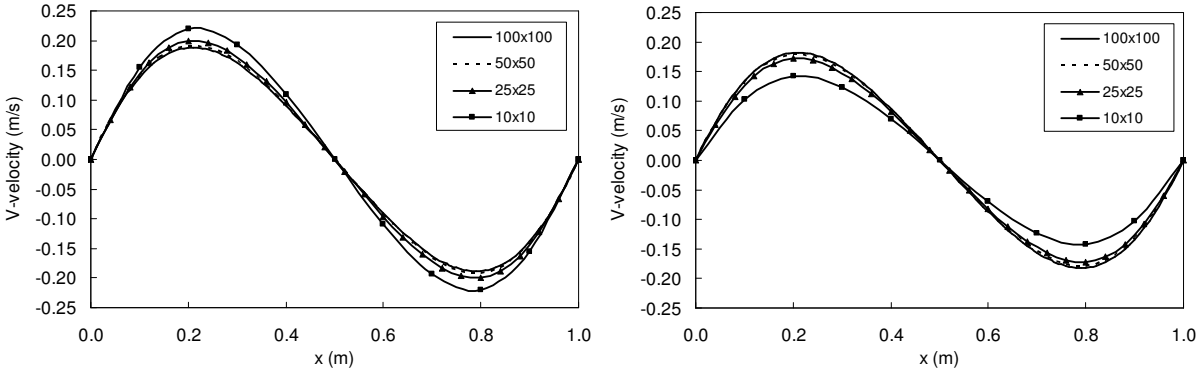

(a) Method 1 (b) Method 2

Figure 5 (a,b): Velocity profiles at $y = 0.5$ for 10x10, 25x25, 50x50, 100x100.

Next we investigate the pressure solution. Plotting the pressure along the cavity centreline $y = 0.5$, Figure 6 (a, b) again shows that the pressures appear to converge, though the solutions at the boundaries are sensitive to the number of particles used, possibly indicating problems with the supposed zero gradient condition at the walls. Again, the results for Methods 1 and 3 are similar.

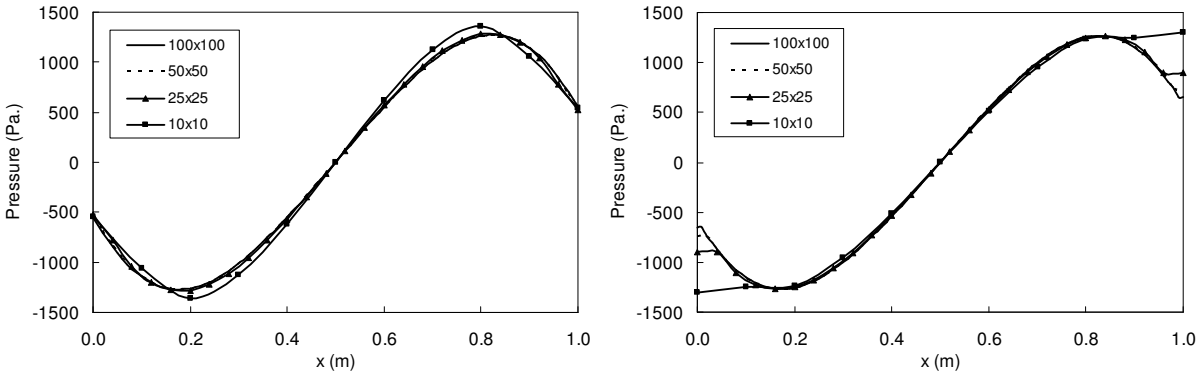

(a) Method 1 (b) Method 2

Figure 6 (a,b): Pressure profiles at $y = 0.5$ for 10x10, 25x25, 50x50, 100x100.

To investigate this further, we look at the pressure gradient along the bottom wall. We choose this because of the presence of singularities in the top two corners due to the discontinuous velocities there. These singularities lead in principle to infinite pressures in these regions thus the numerical pressure solutions (and therefore the resulting gradients) can be expected to be unreliable there. In contrast, the pressure along the bottom wall (and its gradient) should be smooth and predictable. Figure 7 (a, b) demonstrates clearly that none of the methods used here in fact specify the zero-gradient condition effectively (again, Method 3 results similar to those from Method 1). Furthermore the pressure gradient appears to converge to a non-zero value when the number of particles is increased. However, the results indicate that the pressure solution also appears to converge both at and away from the walls.

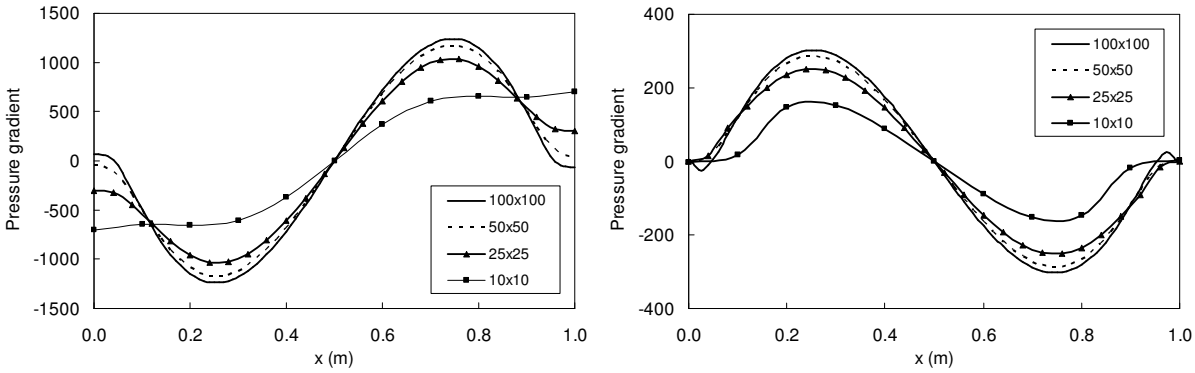

(a) Method 1 (b) Method 2

Figure 7 (a,b): Pressure gradient ($\partial P / \partial y$) profiles at $y = 0$ for 10x10, 25x25, 50x50, 100x100.

In the case where $h = dx$, Methods 1 and 2 force $\partial P / \partial n = 0$ exactly at the first row of dummy particles. With Method 2, the gradient at the wall is approximately zero (and should in principle approach zero as a steady-state is reached, depending on the distance d between the wall particle and the fictitious point from which the pressure is determined). Method 3 sets the gradient to be exactly zero at second line of dummy particles, and approximately at the first line of dummy particles. In the steady state, the boundary conditions from methods 1 and 3 should be identical (as Method 3 is essentially an explicit version of Method 1). If *h* not equal to *dx*, the gradient is effectively zero between first and second rows of dummy particles (methods 1 and 2) and beyond the second line (Method 3). The distance between the physical boundary and the effective boundary reduces as the number of particles n_p increases thus the computed results converge to a final value as n_p is increased.

3.1 GENERAL CONVERGENCE BEHAVIOUR

Figure 8 shows the relationship between the rms error in the SPH solution as a function of the inter-particle distance *dx*. The error is defined as follows. For a given boundary condition method and given *h/dx*, the numerical value for each computation was interpolated to a 100x100 grid. The rms error was then defined as the root-mean-square difference between these interpolated values and the SPH solution using 100x100 particles, for the same boundary condition method and with *h=dx*. Note that Taylor-series analysis reported briefly in section 2.3.4 indicates that in this case SPH should be $O(h^2)$ accurate. In practice, the global convergence rate is approximately $O(h^{1.67 - 1.72})$ [*h=dx*] and $O(h^{1.53 - 1.62})$ [*h*=1.2*dx*]. However, the depressed rate is partially due to the presence of singularities in the upper corners of the lid-driven cavity, which can be expected to have a detrimental effect on convergence. If these corner regions are excluded from our consideration, we can expect better convergence. We also note that, as a consequence of the analysis mentioned briefly at the end of section 2.3.4, the fully-converged solutions for *h=dx* may actually be different from those for *h*=1.2*dx*. In practice, it appears that the converged solutions for both cases are very close (for example, the global rms error for 100x100 case, *h*=1.2*dx* vs *h=dx* is less than 0.1%).

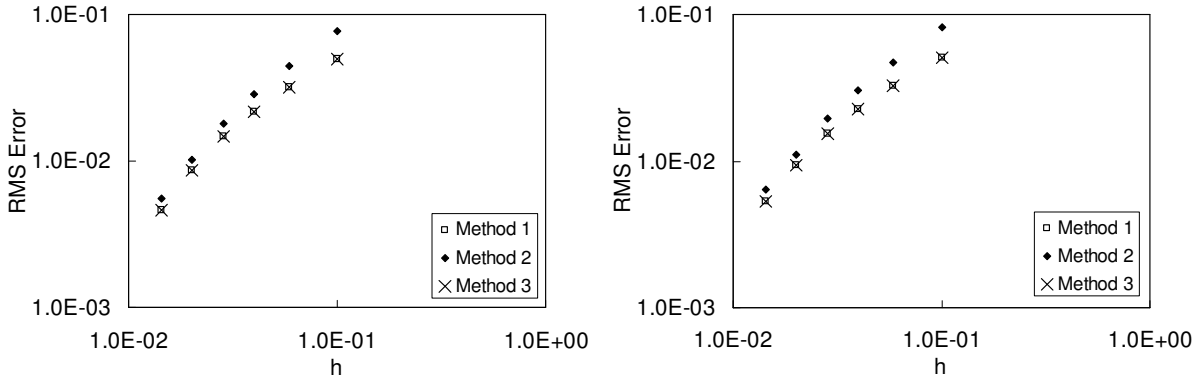

(a) $h = dx$ (b) $h = 1.2\,dx$

Figure 8 (a,b): Steady-state errors: frozen field 10x10, 17x17, 25x25, 35x35, 50x50, 70x70, 100x100: 2x3 cases (a) $h = dx$, (b) $h = 1.2\,dx$. Use 100x100 from $h = dx$ as reference results.

Tables 1 a,b indicate the rms error for the velocity components on the $y = 0.5$ line. The rms error is expressed as the rms difference between computed results for a given discretization (10x10 up to 100x100) compared with the results using the same boundary method with $h/dx = 1$ and using 100x100 particles. This exercise was carried out for the three boundary implementations (methods 1, 2, 3), and two smoothing distance to inter-particle distance ratios ($h/dx =$ 1, 1.2) as reported in Tables 1 a, b. When the singularities are excluded, the convergence rates are approximately O($h^{1.79\ -\ 2.11}$) [h=dx] and O($h^{1.74\ -\ 2.11}$) [h=1.2dx].

	Method 1		**Method 2**		**Method 3**	
Particles	**U**	**V**	**U**	**V**	**U**	**V**
10x10	3.82E-02	2.27E-02	3.33E-02	2.81E-02	3.82E-02	2.27E-02
17x17	2.00E-02	1.28E-02	1.50E-02	1.25E-02	2.00E-02	1.28E-02
25x25	1.21E-02	7.86E-03	8.58E-03	6.98E-03	1.21E-02	7.86E-03
35x35	7.46E-03	4.88E-03	4.96E-03	3.95E-03	7.46E-03	4.88E-03
50x50	4.01E-03	2.64E-03	2.62E-03	2.04E-03	4.01E-03	2.64E-03
70x70	1.72E-03	1.14E-03	1.44E-03	1.09E-03	1.72E-03	1.14E-03
100x100	0.00E+00	0.00E+00	0.00E+00	0.00E+00	0.00E+00	0.00E+00

Table 1a: RMS errors in u and v velocity components for $h/dx = 1$

	Method 1		**Method 2**		**Method 3**	
Particles	**U**	**V**	**U**	**V**	**U**	**V**
10x10	3.76E-02	2.06E-02	3.68E-02	3.16E-02	3.76E-02	2.06E-02
17x17	2.01E-02	1.23E-02	1.64E-02	1.40E-02	2.01E-02	1.23E-02
25x25	1.24E-02	7.72E-03	9.35E-03	7.17E-03	1.24E-02	7.72E-03
35x35	7.71E-03	4.85E-03	5.40E-03	3.80E-03	7.71E-03	4.85E-03
50x50	4.21E-03	2.65E-03	2.88E-03	1.71E-03	4.21E-03	2.65E-03
70x70	1.85E-03	1.14E-03	1.62E-03	6.82E-04	1.85E-03	1.14E-03
100x100	1.48E-04	1.59E-04	1.24E-04	5.33E-04	1.48E-04	1.59E-04

Table 1b: RMS errors in u and v velocity components for $h/dx = 1.2$

CONCLUSIONS

Results have been presented for velocities and pressures computed from incompressible SPH (I-SPH) simulations of the lid-driven cavity flow at very low Reynolds number. In this case, the particle configuration can be fixed and the method can be studied as a traditional grid method. We have investigated the influence of three different implementations of the zero normal gradient condition for the pressure Poisson equation that arises in the I-SPH formulation. We have found that none of the methods used actually enforce the condition exactly at the wall, but argue that each enforces the conditions exactly at some location 'behind' the wall. Of the three methods used, explicit Method 2 is most effective at enforcing the condition and Methods 1 and Method 3 are equally effective as the latter two methods give essentially the same results. Method 1, an implicit method that solves to the wall, may be less prone to instabilities that could potentially arise from using explicit boundary conditions as in Methods 2 and 3. The location where the gradient is exactly zero is further behind the wall for larger values of *h/dx*. Irrespective of the condition used, however, the results appear to converge to the same solution. A convergence study for discretizations between 10x10 and 100x100 shows that global convergence is between $O(h^{1.67 - 1.72})$ [h=dx] and $O(h^{1.53 - 1.62})$ [h=1.2dx]. In regions away from the top corners (at which singularities occur), convergence is $O(h^{1.79 - 2.11})$ [h=dx] and $O(h^{1.74 - 2.11})$ [h=1.2dx].

ACKNOWLEDGMENT

We would like to thank Songdong Shao for making the original version of his I-SPH available to researchers at the University of Plymouth. Jason Hughes has been funded by the Faculty of Technology of the University of Plymouth.

REFERENCES

Chorin A.J. (1967). "A numerical method for solving incompressible viscous flow problems", *J. Comp. Phys.*, **2:** 12-26.

Cleary P.W., Ha J., Alguine V., Nguyen T. (2002). "Flow modelling in casting processes", *Applied Mathematical Modelling*, **26**: 171-190.

Cummins S.J. & Rudman M. (1999). "An SPH projection method", *J. Comp. Phys.*, **152 (2)**: 584-607.

Lee E.-S., Laurence D., Moulinec C., Stansby P., Violeau D. (2006). "Development of an Incompressible SPH Method through SPARTACUS-2D", 1st SPHERIC Workshop, Rome.

Monaghan J.J. & Kos A. (1999). "Solitary waves on a Cretan beach", *ASCE J. of Waterways, Port, Coastal and Oc. Eng.*, **125 (3)**:145-154.

Morris J.P., Fox P.J., Zhu Y. (1997). "Modeling low Reynolds number incompressible flows using SPH", *J. Comp. Phys.*, **136**: 214-226.

Press W.H., Teukolsky S.A., Vetterling W.T., Flannery B.P. (1992). Numerical Recipes in Fortran 77, Cambridge University Press.

Rogers B., Lee E.-S., Violeau D., Quinlan N., Lastiwka M., Basa M. (2006). "Benchmark Case 3: Lid-Driven Cavity Flow", 1st SPHERIC Workshop, Rome. http://wiki.manchester.ac.uk/spheric/images/SPHERIC_newsletter_issue-2.pdf, (pp7-8).

Shao S., Ji C., Graham D.I., Reeve D.E., James P.W., Chadwick A.J. (2006). "Simulation of wave overtopping by an incompressible SPH model", *Coastal Engineering*, **53(9):** 723-735.

Shao S., Lo E.Y.M. (2003), "Incompressible SPH method for simulating Newtonian and non-Newtonian flows with a free surface", *Adv. In Water Resources*, **26**: 787-800.